In Situ Observation of the Precipitation, Aggregation, and Dissolution Behaviors of TiN Inclusion on the Surface of Liquid GCr15 Bearing Steel

QIANREN TIAN, GUOCHENG WANG, DELI SHANG, HONG LEI, XINGHU YUAN, QI WANG, and JING LI

In this study, the precipitation, aggregation, and dissolution behaviors of TiN inclusions on the surface of liquid GCr15 bearing steel have been investigated by combining the observations of confocal laser scanning microscope (CLSM) and field emission scanning electron microscope (FE-SEM) with those obtained from energy dispersive spectrometer (EDS) and theoretical analysis. The kinetic results show that the initial concentration of Ti and N are 0.0078 and 0.0049, respectively, the precipitation temperature is between 1640 K and 1680 K (1367 °C and 1407 °C), and the local cooling rate is between 0.5 and 10 K/s; TiN inclusion can precipitate only when the solid fraction is higher than 0.847 and its precipitation radius is between 1 and 6 μm. The precipitation radius of a TiN inclusion in the GCr15 bearing steel sheet can be reduced by decreasing the N content and increasing the cooling strength. The aggregation and densification of multi-particle aggregated TiN inclusions are verified by CLSM observation and theoretical analysis. The inclusions are aggregated by the cavity bridge force (CBF), and the aggregated TiN is formed by solid-phase sintering. The results of force analysis show that CBF plays a dominant role in the aggregation process of the inclusions. The atomic ratio of Ti and V obtained by EDS is 18:1, which may melt TiN and form the liquid inclusion at 1688 K (1415 °C) observed by CLSM. The theoretical analysis is conducted for the dissolution of the TiN inclusions observed by CLSM, which shows that the dissolution of the TiN inclusions is related to the size of the inclusions; the larger the size, the greater the dissolution rate. The long-strip TiN inclusion may be formed by the Ostwald ripening of two TiN inclusions. The TiN inclusions smaller than 3 μm in the GCr15 bearing steel may be formed by the dissolved Ti and N generated by the dissolution of TiN.

QIANREN TIAN and XINGHU YUAN are with the School of Materials and Metallurgy, University of Science and Technology Liaoning, Anshan, 114051 Liaoning, P.R. China. GUOCHENG WANG, QI WANG, and JING LI are with the School of Materials and Metallurgy, University of Science and Technology Liaoning and also with the Key Laboratory of Chemical Metallurgy Engineering Liaoning Province, University of Science and Technology Liaoning, Anshan, 114051 Liaoning, P.R. China. Contact e-mail: wang_guocheng@163.com DELI SHANG is with the State Key Laboratory of Metal Material for Marine Equipment and Application, Anshan, 114051 Liaoning, P.R. China. HONG LEI is with the Key Laboratory of Electromagnetic Processing of Materials, Ministry of Education, Northeastern University, Shenyang, 110004 P.R. China.

I. INTRODUCTION

THE GCr15 bearing steel is one of the most widely used high-carbon chromium steels. It has strict requirements for the content, microstructure, and purity of steel because of its special usage and service environment. The non-metallic inclusions are the undesired second-phase particles in the GCr15 bearing steel ingot. The content and distribution of inclusions have a great influence on the service life of the bearing steel; the higher the amount of inclusions, the shorter the life. With the continuous improvement of the smelting technology, the control of oxide inclusions in the smelting process has been significantly improved. However, it is still difficult to control some inclusions, such as TiN and MnS, which precipitate during solidification.[1,2] The TiN inclusion is one of the most dangerously rigid inclusions in the GCr15 bearing steel. Fatigue cracks are easily caused during the usage and rolling process in bearing steel because of the hardness

and poor deformability of the TiN inclusions.[3] A large-sized TiN is greatly harmful to the quality of steel, whereas fine TiN can significantly improve the microstructure and properties of the heat-affected zone (HAZ) of the welded steel. Therefore, it is considered to be a kind of inclusion that can play the role of an *oxide metallurgy* inclusion.[4–7] Kanazawa *et al.*[8] observed that fine TiN particles could significantly increase the strength of the HAZ of a weld steel. Tomita *et al.*[9] used the method of adding TiN-MnS composite precipitates to improve the strength of the HAZ in ultralow-carbon steel. TiN can induce the precipitation of acicular ferrite (AF) and nail the grain boundary to prevent the coarse grain.[10,11] TiN can induce MnS inclusion precipitation during solidification, which is a good heterogeneous nucleation site of AF due to its poor manganese area around it.[12] However, in low-carbon steel, TiN will dissolve at a temperature higher than 1623 K (1350 °C) and lose its effect as the *oxide metallurgy* inclusion,[13,14] because the effective size of an *oxide metallurgy* inclusion is considered to be 0.2 to 3 μm.[15] Therefore, keeping the size of the TiN inclusion within 0.2 to 3 μm is the key in making it play the role of an *oxide metallurgy* inclusion.

The *in situ* observation method is an effective way of observing the aggregation and dissolution of inclusions during solidification. Misra *et al.*[16] used the confocal laser scanning microscope (CLSM) to study the precipitation behavior of TiN inclusions between the interface of stainless steel and CaO-Al$_2$O$_3$-MgO-SiO$_2$ slag. It was observed that TiN does not dissolve easily at the steel slag interface. The morphology of TiN varies with temperature, and TiN precipitates can flow through a liquid surface. Zhang *et al.*[17] employed CLSM to study the effect of TiN inclusion particles on the strength of the HAZ in a low-carbon steel. They observed that TiN inclusions can significantly inhibit austenite growth at 1673 K (1400 °C). Wan *et al.*[18] studied the effect of Al$_2$O$_3$, MnS, and TiN inclusions on the grain refinement and precipitation of AF in the HAZ of a high-strength low-alloy (HSLA) steel. However, there are not many studies on the evolution of TiN inclusions in molten steel. Yang *et al.*[19] observed the dissolution behavior of TiN inclusions in the electroslag remelting (ESR) process of the high-carbon steel GCr15SiMn ingot. They suggested that TiN in a solid-liquid two-phase zone of the electrode would be completely dissolved, and TiN obtained during the remelting process is regenerated during solidification.

In this study, based on our previous study,[20] to verify the aggregation and densification mechanisms and investigate the dissolution behaviors of TiN inclusions, the influence of kinetic conditions on the size of TiN inclusions in the GCr15 bearing steel billet was further analyzed. The aggregation and densification mechanisms of the TiN inclusions were verified by observation using the field emission scanning electron microscope (FE-SEM) with energy dispersive spectrometer (EDS), CLSM, and theoretical analysis. The dissolution and Ostwald ripening behaviors of the TiN inclusions and the formation of long-strip TiN were theoretically and experimentally analyzed.

II. EXPERIMENTAL

A. *Chemical Components Analysis*

The GCr15 bearing steel billet was produced by the BOF-LF-VD-CC process in a foundry, whose thickness was 180 mm. The chemical compositions of the billet were analyzed by chemical methods. The total content of aluminum (Al$_t$), titanium, chromium, and vanadium were measured by inductively coupled plasma-mass spectrometry (ICP-MS). The acid soluble aluminum (Al$_s$) content was measured by the Chromazurol-S spectrophotometric method, and the total oxygen (O$_{(T)}$) and nitrogen contents were measured using a nitrogen-oxygen analyzer (Model: TC600, LECO Corporation).

B. *FE-SEM with EDS and CLSM*

A cylindrical specimen with 8 mm diameter and 3 mm height was cut by a wire-cut electric discharge machine. The specimen was polished and observed using FE-SEM (Model: ZEISS-ΣIGMA HD) with EDS (Model: Oxford-X-Max 50 mm^2). After the FE-SEM observation, the specimen was placed in a corundum crucible with an inner diameter of 8 mm, outer diameter of 9 mm, and height of 3.5 mm, and then the crucible was placed in a CLSM heating furnace (Produced by Lasertec CO. Ltd. in Japan, Model: VL2000DX-SVF17SP). The heating furnace was evacuated using a vacuum pump, and Ar gas was injected into the heating furnace. After heating the specimen, the evolution behaviors of TiN inclusions were observed in the heating condition.

The observation area is approximately 242 × 242 μm. After several heating tests for the GCr15 bearing steel, the heating curve was determined. We observed that the steel grade surface was melting at 1673 K (1400 °C), and the TiN inclusion dissolved when the temperature range is between 1673 K and 1743 K (1470 °C). The temperature control curve of the specimen is shown in Figure 1. Between 0 and 180 seconds, the heating temperature was 40 °C/min to ensure that the crucible
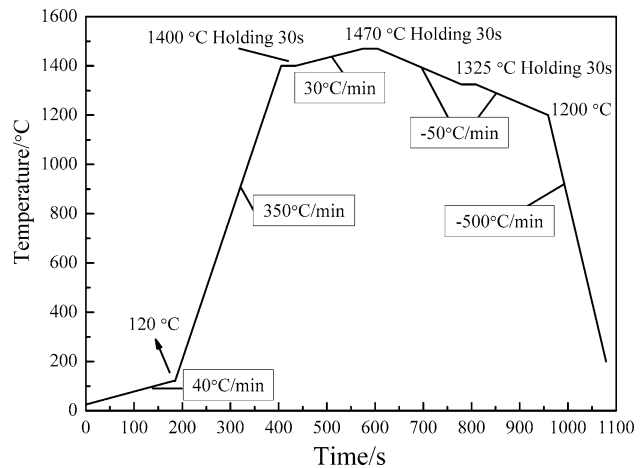

Fig. 1—Temperature controlling profile for *in situ* observation of the inclusion.

does not crack by sudden heating. During this process, when the temperature reached 393 K (120 °C), it holds the temperature for 8 seconds. Further, the heating temperature was set at 350 °C/min to make sure that the TiN inclusion can be observed quickly in a mushy zone of molten steel; this process cost 220 seconds. The solidus temperature of the GCr15 bearing steel is 1603 K (1330 °C), which is calculated in Section IV–A. To observe the motion process and the morphology change of TiN inclusions, the temperature was maintained for 30 seconds. A low heating temperature of 30 °C/min was employed to observe the evolution behavior of the TiN inclusions in the solidification front. When the temperature reached 1743 K (1470 °C), it was maintained for 30 seconds to observe the evolution behavior of TiN inclusions in a temperature higher than the solidus temperature. The multistage cooling method was used to prevent a sudden drop in temperature that could result in the cracking of the crucible. At the first stage, the cooling rate was − 50 °C/min. When the temperature decreased to 1598 K (1325 °C), the temperature was maintained for 30 seconds to observe the surface state of the GCr15 bearing steel during the solidification process. After the observation, the same cooling rate is maintained until the temperature came down to 1473 K (1200 °C). A high cooling rate of − 500 °C/min was used to decrease the temperature of the steel specimen.

III. RESULTS

A. *Chemical Components of GCr15 Bearing Steel*

The concentration of the components in the GCr15 bearing steel billet was obtained by chemical analysis, as shown in Table I. The concentration of Ti and N are more than an average value in a general GCr15 bearing steel, which may increase the number of TiN inclusions. The V content is a little higher than that of Ti, which may make the generation of a solid solution of Ti and V possible. The difference between (Al_t) and (Al_s) is 0.001 mass pct, which means the concentration of the dissolved Al is low in molten steel. Further, $O_{(T)}$ can be controlled in 0.001 mass pct, which also reflects that the deoxidization reaction of Al is good in the smelting process.

B. *Morphologies and Elements Mapping of TiN Inclusions*

The morphologies of TiN inclusions were obtained using the FE-SEM, and the chemical compositions (in atomic percent) and elements mapping of inclusions were acquired using the EDS, as shown in Figures 2 and

3. The inclusions in Figure 2 are named single-particle TiN inclusions, with irregular shape and sharp angles, and their size range is between 2 and 20 μm. The long-strip TiN inclusion in Figure 2(d) has a length of approximately 15 μm. The inclusions in Figure 3 are named multi-particle aggregated TiN inclusions, with strip shape and there are some small inclusions at the tail, and the size is bigger than 20 μm. Such TiN inclusions may be the intermediate state of the aggregation process of multi-particle aggregated TiN inclusion.

According to the chemical compositions and elements mapping of the inclusions, the TiN inclusions are formed not only from T̲i and N̲, but also from V̲, and the ratio of the inclusion in Figure 3(e) is approximately 18:1. This means that both single-particle and multi-particle aggregated TiN inclusions may be the solid-solute inclusions, *i.e.*, (Ti,V)N inclusions. To clarify the formation mechanism of such TiN inclusion, it is necessary to study its evolution behavior in a high temperature using the CLSM.

C. *Precipitation, Aggregation, and Dissolution Behaviors of the TiN Inclusion*

In the heating process produced by CLSM, the evolution behaviors of the TiN inclusions (the inclusions in Figure 3(e)) are shown in Figure 4. The heating process of the specimen began at 298 K (25 °C), and the TiN inclusions observed by the FE-SEM are named A and B1, respectively, and shown in Figure 4(a). Based on the morphologies and size of inclusions A and B1, and the scratch shown in both Figures 3(e) and 4(a), it is easy to discern that A and B1 are the solid-solute (Ti,V)N inclusions.

When the temperature reaches 1618.8 K (1345.8 °C), the heating time is 358.84 seconds, and the surface of the bearing steel gradually melts from the grain boundary (GB). The sharp angle at the right side of inclusion A separates the GB on the surface of steel, as shown in Figures 4(b) and (c). This phenomenon suggests that the TiN inclusion plays the role of pinning the GB. With temperature rising to 1680.6 K (1407.6 °C), the heating time is 389.13 seconds, and the surface of steel around inclusions A and B1 gradually melts until they are completely exposed between the interface of the GCr15 bearing steel and Ar gas, shown in Figure 4(d). When the temperature is 1680.5 K (1407.5 °C), the heating time is 389.45 seconds, on the right side of inclusion B1, there is an inclusion formed by element diffusion, B2, as shown in Figure 4(e). It is not obvious because the inclusion is not large in quality and size, and the pressure on the inclusion B2 is not significant. With the continuous diffusion of elements, it gradually grows up.

Table I. Chemical Components of the GCr15 Bearing Steel Billet (in Mass Percent)

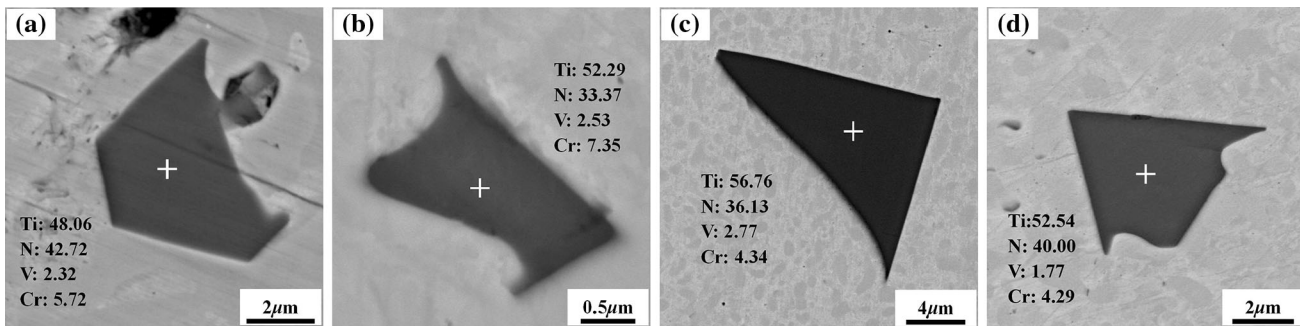| Component	C	Si	Mn	P	S	Ti	Cr	V	N	Als	Alt	Ca	$O_{(T)}$
Concentration	1.01	0.25	0.36	0.012	0.0014	0.0078	1.46	0.0099	0.0049	0.011	0.012	< 0.005	0.0009

Fig. 2—Typical single-particle TiN inclusions in the GCr15 bearing steel. (*a*), (*b*), (*c*), and (*d*) are the inclusions with chemical compositions (in atomic percentage).
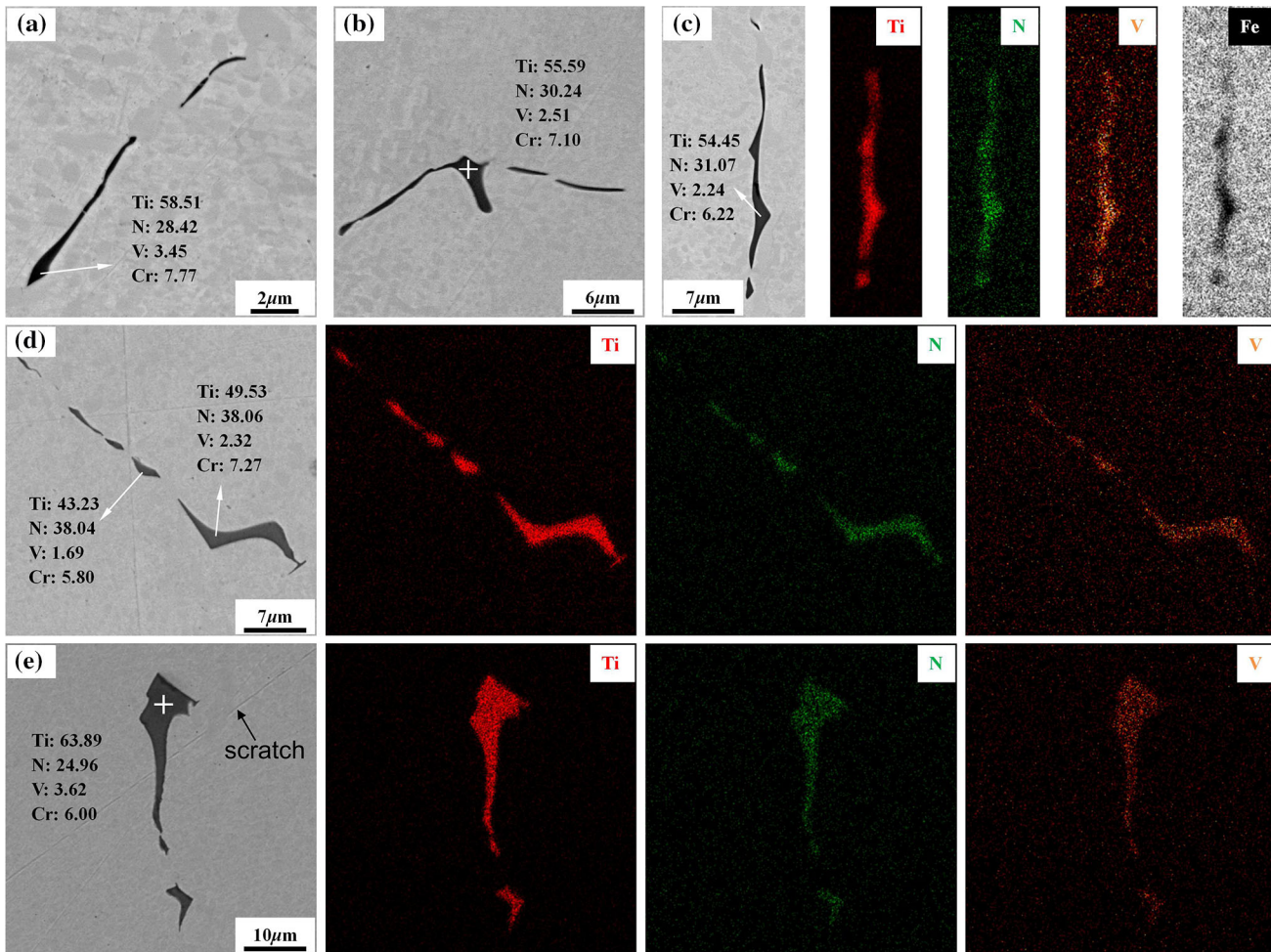

Fig. 3—Morphologies, chemical compositions (in atomic percentage), and elements mapping of the multi-particle aggregated TiN inclusions. (*a*) and (*b*) are the inclusions with chemical compositions; (*c*), (*d*), and (*e*) are the inclusions with chemical compositions and elements mapping.

In Figure 4(f), the long-strip inclusion B2 can be observed, with a length of approximately 10 μm. At this time, the distance between inclusions A and B1 is obviously less than that between B1 and B2. However, with the movement of the inclusions on the molten steel surface, inclusion B1 gradually moves to B2 and fuses with it to form the inclusion B at 401.82 seconds. The size of the inclusion B is larger than B2, with a length of approximately 17 μm. The movement process is shown

in Figures 4(g) and (h). As the heat preservation process was conducted, at the heating time of 406.74 seconds, an inclusion named C under the liquid steel floats to the surface with a steady geometry state due to the effect of buoyancy, as shown in Figure 4(i). According to the morphology of inclusion C, it is similar to the inclusion observed in Figure 2(a); therefore, inclusion C may be a TiN inclusion. As shown in Figure 4(j), inclusion C has the shape of convex, and it connects with the tail of
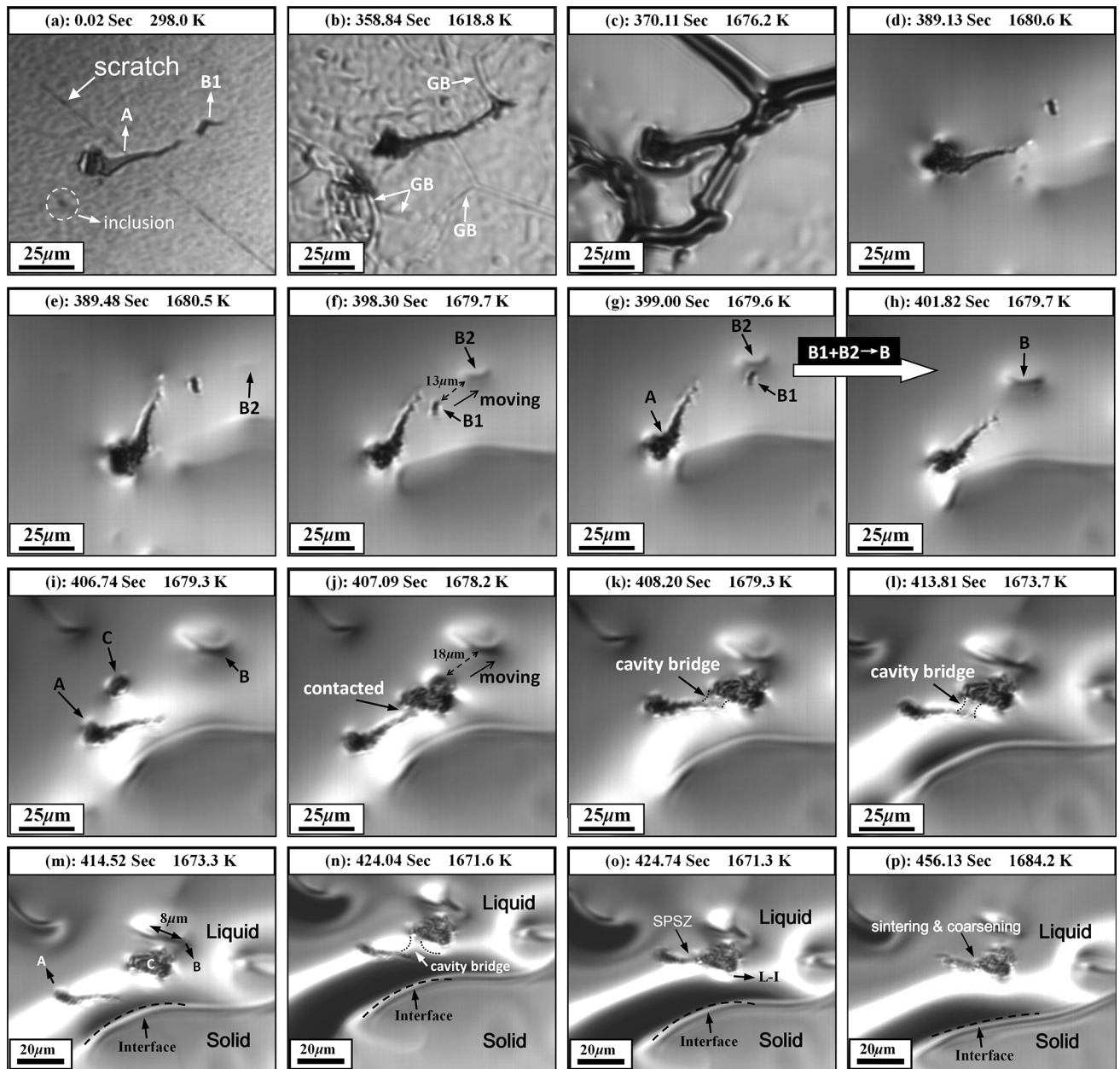
Fig. 4—Aggregation process of TiN inclusions observed by CLSM. (*a*) through (*d*) Melting process of the matrix. (*e*) and (*f*) Precipitation process of inclusion B2. (*g*) through (*p*) Aggregation process of inclusions A and C.

inclusion A in a short time. The aggregated inclusion is named inclusion A + C. The inclusion A + C has the tendency of moving toward inclusion B. At 408.20 seconds, the temperature is 1679.3 K (1406.3 °C), the top of inclusion C contacts with inclusion B, and the left angle connects with inclusion A forming a shadow area, which is called a cavity bridge, as shown in Figure 4(k). Under the influence of temperature fluctuations, the temperature in the heating furnace is reduced. The surface tension of the molten steel in the liquid phase increases, and the cavity bridge becomes slender, as shown in Figure 4(l). At 414.52 seconds, the temperature is 1673.3 K (1400.3 °C), and the cavity bridge

between inclusions A and C breaks up, as shown in Figure 4(m). When the temperature is restored to a stable state, a cavity bridge will be formed between inclusions A and C. The cavity bridge will induce the tail of inclusion A to be close to inclusion C, and the contacted part of inclusions A and C will form a solid-phase sintering zone (SPSZ).[20] At this time, there is a small amount of liquid inclusion (L-I) on the right side of inclusion C, which may be the solid-solution L-I, and this process can be seen in Figures 4(n) and (o). The inclusions A and C continue to be sintered and coarsened as inclusion A + C in SPSZ, as shown in Figure 4(p).
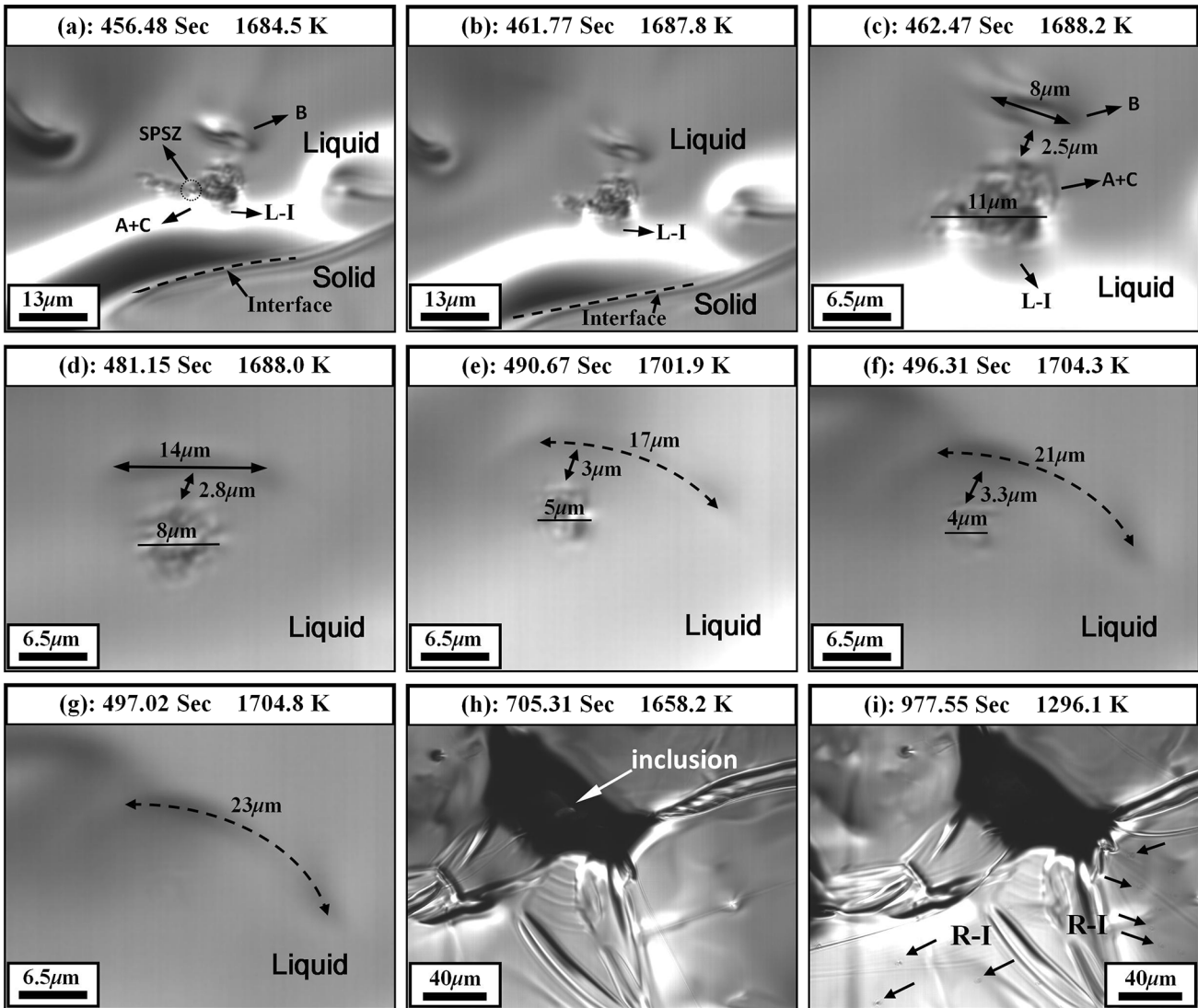
Fig. 5—Dissolution behavior of TiN inclusions observed by CLSM. (*a*) through (*c*) Dissolution process of inclusion A. (*c*) through (*g*) Dissolution process of inclusion A + C. (*h*) and (*i*) Solidification of matrix and reprecipitation behaviors of R-I.

The dissolution process of inclusion A is shown in Figures 5(a) through (c), and the temperature change is only 4 K. At 462.47 seconds, inclusion A is completely dissolved; at the same time, there are some L-I appearing at the right side of inclusion C. It can be inferred that the L-I may be the liquid phase of the (Ti, V)N inclusion. As the temperature increases, the edge of inclusion A + C continues to dissolve, the size of inclusion A + C gradually decreases, and its distance with inclusion B increases. The morphology of inclusion B changes from ellipse to a long strip, and the size increases. When the inclusion A + C completely disappears, the length of inclusion B can reach approximately 23 μm, and the dissolution process of inclusion A + C is shown in Figures 5(c) through (g). In the subsequent cooling process, the long-strip TiN-contained inclusion is separated from the observation field due to the significant fluctuation of the liquid surface. Without changing the field of view, a large inclusion of unknown

composition is formed during the cooling process, which results in the formation of a cavity in the process, as shown in Figure 5(h). When the temperature drops to 1296.1 K (1023.1 °C), as shown in Figure 5(i), there are some reprecipitated inclusions (R-I) around the cavity.

IV. DISCUSSION

A. *Precipitation Kinetics of TiN Inclusion*

The reaction equation for the precipitation of TiN inclusions can be expressed as follows:

$$[\text{Ti}] + [\text{N}] = \text{TiN}_{\text{inclusion}}. \qquad [1]$$

According to the concentration of the components in the billet, employing the calculation parameters and equations in the previous study,[20] the solidus and liquidus temperatures (1603 K and 1724 K [1330 °C and

1451 °C]), the precipitation solid fraction of TiN inclusions (0.847), and its corresponding temperature of 1640 K (1367 °C) can be obtained, respectively.

Based on the nucleation work equation of inclusions, Eq. [2],[21] the precipitation of TiN inclusions is determined by the degree of supercooling (from the precipitation temperature of TiN inclusion) and the supersaturation (S^*) of the dissolved elements in the cooling process. According to equilibrium partition coefficient of $\underline{Ti}$ and $\underline{N}$ ($k_{Ti} = 0.33$ and $k_N = 0.48$),[22,23] Ti and N are the positive segregation elements, and they can constantly enrich the solidification front that leads to an actual concentration product, Q_{TiN}, being greater than the theoretical concentration product of TiN inclusion, K_{TiN}. Therefore, the supersaturation ($S^* = Q_{TiN}/K_{TiN}$) in solidification front is definitely greater than 1. That means the degree of supercooling is the main limiting condition for the nucleation of the TiN inclusion. The relationship between the degree of supercooling and the local cooling rate R_c in solidification front can be expressed as Eq. [3].[24]

$$\Delta G^* = \frac{16\pi}{3} \times \frac{\gamma_{PL}^3 V^2}{(R\Delta T \ln S^*)^2} \qquad [2]$$

$$\frac{d\Delta T}{dR_c} = \frac{\Delta T}{R_c \times \left(1 + \frac{Af(\theta)\gamma_{PL}^3 T_l^2}{\Delta H_V^2 \kappa} \times \frac{2T_l - 3\Delta T}{\Delta T^2(T_l - \Delta T)}\right)}, \qquad [3]$$

where ΔG^*, γ_{PL}, V, R_c, A, $f(\theta)$, ΔH_V, κ, and T_l denote Gibbs nucleation free energy, interfacial energy between inclusion and liquid Fe, molar volume (cm^3 mol^{-1}), local cooling rate, nucleus shape factor ($3/16\pi$ for a spherical nucleus), catalytic factor, heat of fusion, Boltzman constant (1.38×10^{-16} erg K^{-1}), and liquidus temperature of steel, respectively.

In a continuous casting process of slab, the secondary arm spacing is generally between 200 and 500 μm. When it is 200 μm, R_c is 0.5 K/s, and the relationship between the secondary arm spacing L and R_c can be expressed as Eq. [4].[25] In the thin slab continuous casting process, the secondary arm spacing is between 52 and 180 μm, when the average secondary arm spacing is 99 μm, the cooling rate is approximately 5 K/s.[26] R_c is set as 0.5, 1, 5, and 10 K/s, which covers the range of actual local cooling rate, and is suitable to discuss the precipitation law of TiN inclusion under different degrees of supercooling and precipitation temperature. According to the chemical compositions of the billet and the determined R_c, combining with the calculated temperature (1640 K) and the precipitation temperature (1680 K) of inclusion B2 observed by CLSM, the precipitation temperature used to calculate the radius of TiN particle were set as 1640 K, 1660 K (1387 °C), and 1680 K. The theoretical precipitation radius of the TiN inclusion can be expressed as Eq. [5], and the relationship between the radius and the solidification fraction is shown in Figure 6 (the unit of r was converted from cm to μm). τ denotes the local cooling time, s, which is described by Eq. [6].
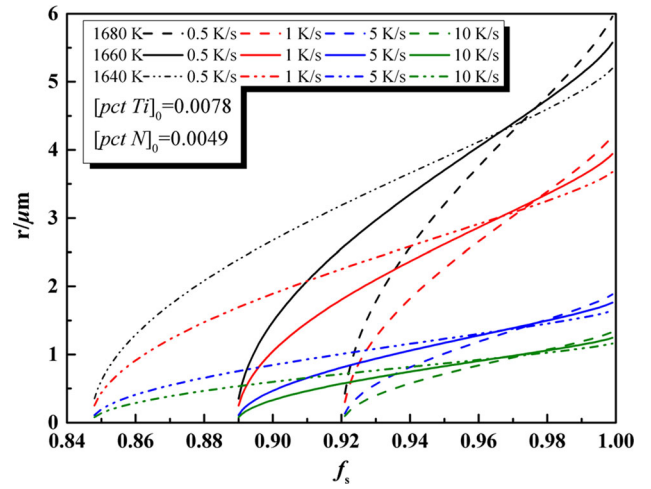

Fig. 6—Relationship between the precipitation radius of particles and the solid fraction at different precipitation temperatures and local cooling rates.

$$L = \begin{cases} (169.1 - 720.9 \times [pct\ C]) \times R_c^{-0.4935}, & (0 < [pct\ C] \le 0.15) \\ 143.9 \times [pct\ C]^{(0.5501 - 1.996[pct\ C])} \times R_c^{-0.386}, & ([pct\ C] > 0.15) \end{cases}$$
$$[4]$$

$$r = \sqrt{\frac{M_s}{50 M_m} \times \frac{\rho_m}{\rho_s} \times D_N \times ([pct\ N]_L - [pct\ N]_e) \times \tau}$$
$$[5]$$

$$\tau = \frac{T_l - T_s}{R_c}, \qquad [6]$$

where r, M_s, and M_m denote the radius of the particle (cm), molar mass of TiN (62 g/mol), and molar mass of melting steel (56 g/mol), respectively. ρ_s and ρ_m denote the density of TiN (5.43 g/cm^3) and density of molten steel (7.07 g/cm^3); D_N denotes the diffusion coefficient of $\underline{N}$ in molten steel, 3.91×10^{-6}, 4.54×10^{-6}, and 5.25×10^{-6} cm^2/s for 1640 K, 1660 K, and 1680 K, respectively; $[pct\ N]_L$ and $[pct\ N]_e$ denote the mass fraction of $\underline{N}$ during the solidification of molten steel and the mass fraction of $\underline{N}$ in equilibrium with TiN (mass pct), respectively; R_c is the local cooling rate (K/s); T_s and T_l denote the solidus and liquidus temperatures (K) respectively.

The calculation results show that at the same local cooling rate, with the precipitation temperature of TiN decreasing, the precipitation of TiN size increases due to the increase of TiN inclusion precipitation at a low temperature. At the same precipitation temperature, with the decreasing of local cooling rate, the precipitation size of TiN increases, because the TiN inclusion precipitated at low solid fraction gradually grows up. When the solid fraction approaches the value 1 and the local cooling rate is 10 K/s, the minimum precipitation

radius of the TiN inclusion is approximately 1 μm. When the local cooling rate is 0.5 K/s, the maximum precipitation radius of the TiN inclusion is approximately 6 μm. In the temperature range between 1640 K and 1680 K, with the precipitation temperature increasing, the growth rate (the slope of growth curve) of the TiN inclusion increases. According to Eq. [2], in the determined compositions of the molten steel, the radius of the TiN inclusion is mainly decided by the concentration and diffusion coefficient of N. Furthermore, in the same temperature condition, the diffusion efficiency of N is greater than that of Ti. For instance, when the temperature comes down to 1680 K, the diffusion coefficients of N and Ti are 5.25×10^{-6} and 2.36×10^{-9} cm^2/s in γ-phase ($D_{Ti}^{\gamma} = 0.15\exp(-250956/RT)$ and $D_N^{\gamma} = 0.91\exp(-168490/RT)$[2]), respectively. Thus, the growth rate of the TiN inclusion is related with the kinetic conditions of the molten steel, and the most important condition is the diffusion of N. When the local cooling rate ranges between 0.5 and 10 K/s, the radius of TiN inclusion ranges between 1 and 6 μm. This is consistent with the size of the single-particle TiN inclusions observed by FE-SEM. After the solid fraction of the molten steel is greater than 0.847, the TiN inclusion can precipitate in GCr15 bearing steel. Therefore, the final size of TiN can be reduced by reducing the concentration of Ti and N (mainly reducing the content of N) and increasing the solidification rate.

B. *CBF Mechanism of TiN Inclusion Aggregation*

According to the observation of the TiN aggregation process, as shown in Figure 4, it is concluded that the aggregation process contains three stages: the inclusions are adsorbed and aggregated by the cavity bridge force (CBF) generated due to the cavity bridge; collision coarsening occurs around the neck region of the aggregated inclusions; and inclusions and new precipitates are sintered in a solid-phase state. The schematic diagram of the aggregation process of two isodiametric sphere particles with sharp angles is shown in Figure 7. The initial stage is based on the cavity bridge theory proposed by Sasai.[27,28] Two single-particle TiN inclusions are present: one is the host inclusion, which does not move on the surface of the liquid steel, and the other is the guest inclusion, which has a moving velocity of V_G. At a determined distance d (depended on the radius of inclusions, R_p), expressed as Eq. [7], a cavity bridge without liquid steel will be formed between the two inclusion particles. Under the influence of the cavity bridge, a CBF will be formed between the two inclusion particles. During aggregation, the radius of curvature of the cavity decreases and CBF increases continuously. The coefficient of CBF increases from 1.54 to 1.88. In aggregation, the moving state of inclusion keeps it moving in the way of minimum resistance. Therefore, due to the angles of TiN inclusions, the most ideal collision way is the angle collision. This is in agreement with the experimental phenomena observed in CLSM, which are shown in Figures 4(j) through (o). The

aggregation time of inclusions is very short because of the dominant effect of CBF provided by the cavity bridge. As shown in Figures 4(n) and (o), the time is only of 0.7 seconds; thus, the precipitation of TiN during the movement of elements is weak during such a short movement, and it is unobservable in CLSM.

The intermediate stage: when two TiN inclusions collided due to the influence of molten steel surface tension and the low wettability between the molten steel and TiN inclusions, a tiny cavity between the inclusions and molten steel will form. The instantaneous velocity of the guest inclusion becomes V_G'. This is consistent with the experiment reported by Nakamoto,[29] as shown in Figure 7(b). Due to the continuous aggregation of Ti and N in the solidification front, a large number of Ti and N can enrich near the cavity, and the nucleation site is around the junctional area of the molten steel, cavity, and inclusions. The difference in the internal components of the two inclusions causes the solid-phase sintering to occur between the two inclusions. Lumley *et al.*[30] and Xuan *et al.*[31] reported the angle contact solid-phase sintering phenomenon. The angle contact sintering phenomenon resulted in the disappearance of the cavity, while the newly precipitated TiN growing in the neck region of the two inclusions (the green parts in Figures 7(c) and (d)) denotes the newly precipitated TiN. The common velocity of host and guest inclusions is V_{H+G}. There is a certain concentration difference between each phase, which makes the concentration transfer of Ti and N between each phase to occur, and the mass transfer paths of Ti and N are shown as white lines in Figure 7(d). The phenomenon of the TiN inclusion nucleation around the cavity is collision coarsening, which can be observed in CLSM, as shown in Figure 4(p).

The final stage: as TiN inclusion constantly precipitates in the neck region of the inclusions, it will grow until it becomes a stable arc surface, which is formed by the interfacial tension of molten steel and inclusions. There is a concentration difference among the newly precipitated TiN, the host inclusion and the guest inclusions, and the solid-phase sintering reaction (SPSR)[20] will occur to form a stable connected TiN inclusion, which is shown as stage 3 in Figure 7.

In the *in situ* observation, there are two TiN inclusions with different sizes on the surface of the molten steel. A schematic diagram of the action forces of the two inclusions in the SPSR process is shown in Figure 8. In the adsorption process of the two inclusions, the host inclusion is with a radius of R_1 and the guest inclusion is with a radius of R_2. In the mutual movement process, the velocity of guest inclusion V_2 is far greater than that of the host inclusion V_1; thus, V_1 can be ignored as 0. The surface sinking of the molten steel is caused by the formation of CBF, as the shadow part marked in Figures 4(l) and (n). At a certain temperature, the surface tension of the molten steel can be expressed as Eq. [8]. The surface tension of the molten steel is determined to be 2 N/m during the calculation of the aggregation process of inclusions. In the aggregation process, the aggregation force of the single inclusion on
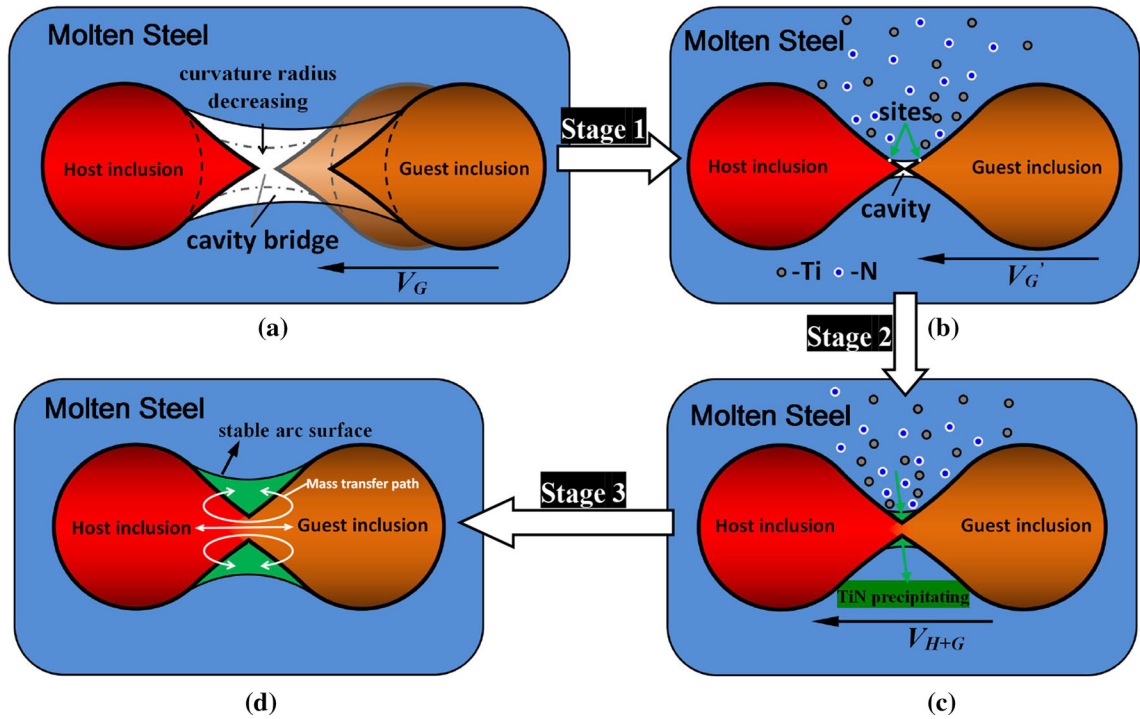
Fig. 7—Schematic diagram of the motion process of spherical inclusions with sharp angles. (*a*) Aggregation process of the two particles, (*b*) precipitation process of T̲i̲ and N̲ in the junctional area, (*c*) precipitation process of Ti and N on the newly precipitated TiN, and (*d*) densification process by SP̲S̲R̲.
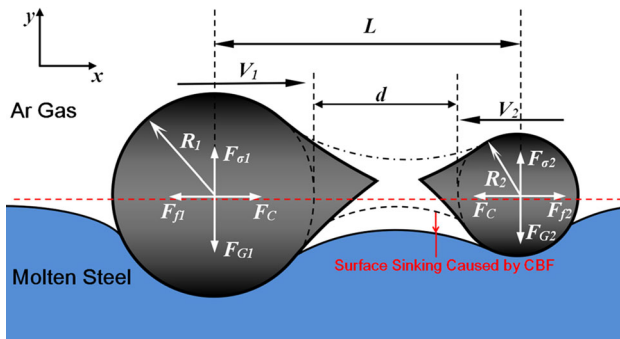

Fig. 8—Schematic diagram of the action force on the different size spherical particles with sharp angles.

the molten steel surface is mainly the CBF (F_C, N), which is expressed as Eq. [9], whose minimum coefficient is 1.54 and the maximum coefficient is 1.88. Without considering the effect of angle on the aggregation of the movement, CBF is proportional to the molten steel surface tension σ_{Fe} and the inter-particle spacing of d. The steel surface resistance impeding the inclusion movement (F_f, N), which is related to the surface viscosity of molten steel, $\mu_{Fe} = 6.7 \times 10^{-3}$ Pa s (Pa = N/m^2),[32] area of the inclusion on the molten steel surface (S, m^2), ratio of the velocity variation in x direction (ΔV_x, m/s), and displacement in the y direction (Δy, m), is expressed as Eq. [10]. The surface tension of the molten steel (F_σ, N), which is the sum action force of tension on the surface, is expressed as Eq. [11]. In molten steel, due to the density difference of inclusion

and molten steel, the surface tension on inclusions is characterized by the buoyancy (F_b, N), as Eq. [12]. The gravity of inclusion (F_G, N) is related to the density of TiN (ρ_{TiN}, Kg/m^3), inclusion volume ($V_{inclusion}$, m^3), and acceleration of gravity (g, N/Kg), which is expressed as Eq. [13]. The force analysis of the inclusion process is conducted under the assumption of two sets of different parameters. The inclusion velocity is determined according to the displacement and time observed in CLSM. The first set is the aggregation process between two isodiametric spherical inclusions with the same diameter, $R_1 = R_2 = 10$ μm and $V_1 = V_2 = 10$ μm/s, and based on the observation results, Δy is approximately 5 μm. The two particles are in the same state of force and motion. The second set is the aggregation of two different size particles, the large size particle radius is 10 μm, $R_1 = 10$ μm, and the small size particle radius is 3 μm, $R_2 = 3$ μm; the corresponding velocities are 0 and 20 μm/s, *i.e.*, $V_1 = 0$ and $V_2 = 20$ μm/s, respectively. F_f is mainly affected by velocity considering the motion particle as a calculation object, that is, the calculation results are the force parameters of R_2. The main action force parameters and results of the particle aggregation process are shown in Table II.

The calculation results show that, under an ideal condition, the CBF between inclusions plays a dominant role in the movement of inclusion particles. The magnitude of CBF is far greater than that of the other forces. Under the non-ideal conditions, F_C, F_σ, and F_f are not strictly distributed in the direction of x or y. For example, F_σ may form an angle of less than or greater than 90 deg with F_C because of the change in

Table II. Summary of Main Action Force Parameters and Results in Particles Motion Process

	Parameters	F_C ($\times 10^{-6}$ N)	F_f ($\times 10^{-12}$ N)	F_σ ($\times 10^{-13}$ N)	F_G ($\times 10^{-9}$ N)
1	$R_1 = 10\ \mu m$, $R_2 = 10\ \mu m$ $V_1 = 10\ \mu m/s$, $V_2 = 10\ \mu m/s$	7.112	8.415	2.228	1.256
2	$R_1 = 10\ \mu m$, $R_2 = 3\ \mu m$ $V_1 = 0$, $V_2 = 20\ \mu m/s$	2.134	1.515	0.060	0.113

temperature. This means that F_σ may play a role in promoting or hindering the adsorption of inclusions. However, the CBF plays a dominant role in magnitude, even if all other forces act as resistance; thus, the dominant role of CBF will not be changed. Further, if the CBF between two inclusions is generated, aggregation and SPSR will occur.

$$d = 0.14R_p \qquad [7]$$

$$\sigma_{Fe} = 2.858 - 0.00051T \qquad [8]$$

$$F_C = (1.54 - 1.88) \times d \times \sigma_{Fe} \qquad [9]$$

$$F_f = \mu_{Fe} S \frac{\Delta V_x}{\Delta y} \qquad [10]$$

$$F_\sigma = \sigma_{Fe} \times S \qquad [11]$$

$$F_b = \rho_{Fe} V_{inclusion} g \qquad [12]$$

$$F_G = m_{TiN} g = \rho_{TiN} V_{inclusion} g. \qquad [13]$$

C. Mechanism of TiN Inclusion Dissolution

Based on the chemical compositions of TiN inclusions, $\underline{Ti}$ and $\underline{V}$ have good solid solubility. From Figures 5(a) through (c), the L-I may be a liquid (Ti,V)N inclusion. The melting point of pure TiN and VN is 3203 K and 2593 K (2930 °C and 2320 °C), respectively.[33,34] The solid-solution stoichiometry ratio of $\underline{Ti}$ and $\underline{V}$ is not determined, and the solid solution of $\underline{V}$ can still affect the melting point of the solid solution. The dissolution process of the TiN inclusion observed by Yang et al.[18] did not show L-I in GCr15SiMn steel, because there is no solid-solution element V in the element mapping and the chemical compositions results of TiN inclusions in their study. Therefore, according to the TiN dissolution process shown in Figures 5(a) through (g), the dissolution behavior of TiN can be summarized as follows. At the left side of inclusion A + C formed after SPSR, inclusion A gradually melts and becomes L-I. Affected by the surface tension of molten steel and the gravity of inclusion C, there will be a ring void formed around inclusion C. After L-I floats into the ring void, inclusion C will be wrapped by L-I and dissolve gradually. In the dissolution process of inclusion A + C, the position with angle will dissolve first, and inclusion A + C becomes a rotundity. Further, it will simultaneously dissolve in all directions. In the heating process, as shown in Figures 5(c) through (g), with the gradual dissolution of inclusion A + C, the length of inclusion B increases gradually. This process is a typical Ostwald ripening phenomenon. In a unit thermal cycle, the specific form of Ostwald ripening mechanism is different in different stage.[35,36] Although the size of inclusion A + C is larger than inclusion B, in the Ostwald ripening process, the diffusion of elements plays a dominating role in the dissolution process, which forms the dissolution of inclusion A + C and the growth of inclusion B. The schematic diagram of the Ostwald ripening process between inclusions B and A + C is shown in Figure 9. As the dissolved elements continuously diffuse to inclusion B, the van der Waals force is formed between inclusions B and C, which makes inclusion A + C moving to the opposite direction of inclusion B. The van der Waals force can be expressed as follows[37]:

$$F_{vw(d_{BC})} = -\frac{A_H r_B r_C}{(r_B + r_C) \times d_{BC}}, \qquad [14]$$

where A_H denotes the Hamaker coefficient, which is a constant (10^{-19}–10^{-20} J) that depends on the material properties (it can be positive or negative in sign depending on the intervening medium); d_{BC} denotes the distance between inclusions B and C; and r_B and r_C denote the radius of inclusions B and C, respectively.

The quantitative model of the Ostwald ripening mechanism is extremely cumbersome, and there are many derivatives for it. As a result, scholars have used different methods to calculate the relationship between the material coarsening, dissolving, and the time. Lifshitz and Slyozov[38] have used a mathematical analysis method to derive the relationship between the particle size and the time in dissolution process.

$$r_t^3 - r_0^3 = \frac{8\sigma V_m^2 D C_s}{9RT} t, \qquad [15]$$

where r_t is the radius of the particle after the reaction time t (cm), r_0 is the radius of the particle before reaction (m), V_m is the molar volume of particle (cm³/mol), $V_{TiN} = 11.53$ cm³/mol; C_s is the mean
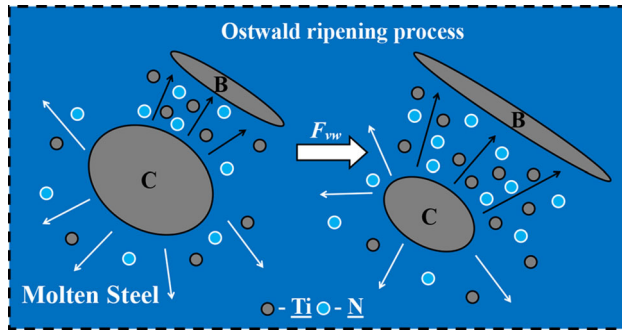
Fig. 9—Schematic diagram of the Ostwald ripening process between the TiN inclusions (the black arrows indicate the diffusion of the elements to inclusion B and the white arrows indicate the diffusion of the elements to molten steel).

solute concentration in the matrix (mass pct), σ is the surface free energy of particle (J/cm^2), D is the diffusion coefficient of elements (cm^2/s), and t is the phase transition time (s). R is the universal gas constant, 8.31 J/(mol K), and T is the absolute temperature (K).

Wagner[39] expressed the Ostwald ripening mechanism as

$$\bar{r}^2 = \frac{64\sigma C_s D V_m^2 k_s}{81 R T l} t, \qquad [16]$$

where $\bar{r}$ is the average radius of particle (cm) and k_s is the reaction rate constant (cm/s).

Aaron[40] expressed the Ostwald ripening mechanism as

$$r_t^2 - r_0^2 = -2 \times \frac{(C_r - C_s) \times D \times t}{C_p - C_r}, \qquad [17]$$

where C_p is the solute concentration in the particle (mass pct) and C_r is the interface concentration of matrix (mass pct).

The kinetic equations mentioned above can be expressed in the following general forms[41]:

$$\frac{dr}{dt} = -\frac{C_r - C_s}{C_p - C_r} \times \left(\frac{D}{r}\right)^n \qquad [18]$$

$$C_k = \frac{C_r - C_s}{C_p - C_r}. \qquad [19]$$

When $C_k > 0$, and C_r is larger than C_s, particles dissolve; when $C_k < 0$, and C is smaller than C_s, particles grow. Moreover, when $C_k = 0$, the process of particle coarsening and dissolution is in equilibrium. Moon et al.[42] reported that the stability of the particles is determined by the temperature of its solid solubility curve. The particle can nucleate and grow at a temperature below the solid solubility curve until their fraction reaches the equilibrium fraction. The coarsening of particle is caused by the decrease of the surface energy between particles. At the same time, the size and distribution of the particle need to be reconsidered. The concentration of solute at the interface corresponds to the concentration of the matrix. That is, the particle is neither coarsened nor dissolved. This size can be defined as the critical particle size at a given temperature:

$$r_{cr} = \frac{2\sigma V_m}{RT} \left(\ln\left(\frac{C_s}{C_\infty}\right)\right)^{-1}, \qquad [20]$$

where r_{cr} is the critical radius of the particle (m) and C_∞ is the equilibrium concentration of solute atoms (mass pct).

In the processes of actual production and in situ observation because the dissolution of (Ti,V)N inclusion is in the temperature-changing environment, the influence of changing temperature on inclusion size cannot be accurately reflected by the methods mentioned above. Therefore, according to the phase transformation law of particle in molten metal,[43–46] under the changing temperature, the relationship among the system temperature, the size of TiN inclusion, and the reaction time was calculated at the determined concentration of Ti and N in GCr15 bearing steel based on the concentration product of Ti and N and Eqs. [21] through [23].

$$[\text{pct Ti}]_{int} = [\text{pct Ti}]_{bulk}$$
$$- \frac{m_{Ti}}{m_N} \left(\frac{D_N}{D_{Ti}}\right)^{\frac{1}{2}} \times ([\text{pct Ti}]_{bulk} - [\text{pct Ti}]_{int})$$
$$[21]$$

$$c^* = \frac{[\text{pct N}]_{bulk} - [\text{pct N}]_{int}}{[\text{pct N}]_{inc} - [\text{pct N}]_{int}} \qquad [22]$$

$$r_{i+1} - r_i = c^* \times \left[\frac{D_N}{r_i} + \left(\frac{D_N}{\pi t}\right)^{\frac{1}{2}}\right] \times \Delta t, \qquad [23]$$

where $[\text{pct Ti}]_{int}$ and $[\text{pct N}]_{int}$ denote the concentration of Ti and N in solidification front of molten steel (mass pct), respectively, $[\text{pct Ti}]_{bulk}$ and $[\text{pct N}]_{bulk}$ denote the concentration of Ti and N in bulk steel (mass pct), respectively, $[\text{pct N}]_{inc}$ denotes the concentration of N in inclusions (mass pct), and Δt denotes the time step of inclusion size from r_i to r_{i+1} (s). The calculation results are shown in Figure 10, and the curves are called time-temperature-transformation (TTT) diagram (d_f is the final size of particle, defined as 1 pct of d_0).

According to Figures 5(c) through (g), the disappearing times of inclusion A + C are 35, 16, 6, and 1 seconds, respectively, from the initial radii of 11, 8, 5, and 4 μm, and the corresponding temperatures are 1688 K, 1688 K, 1702 K, 1704 K, and 1705 K ($r = 0$). According to the TTT curves, their phase transition times are 39, 21, 8, and 4 seconds (difference of time from maximum equilibrium position to corresponding temperature), as shown in Figure 10. The observed phase transformation time is in great consistence with the calculated results, which reflects that the dissolution of TiN inclusion conforms to the Ostwald ripening reaction to a certain extent. In the dissolution process of
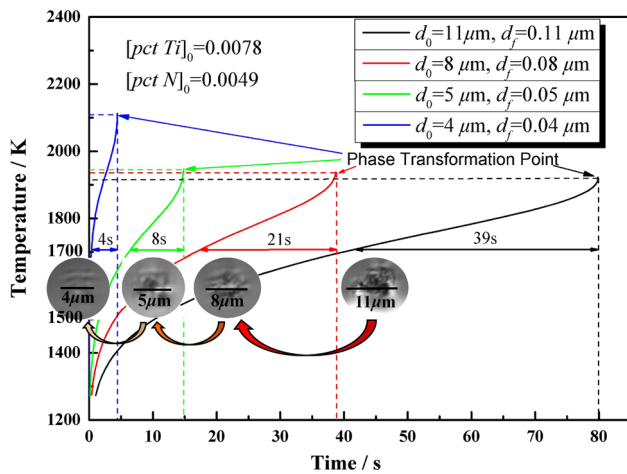
Fig. 10—TTT curves for TiN inclusion, whose d_0 is 11, 8, 5, and 4 μm, respectively.
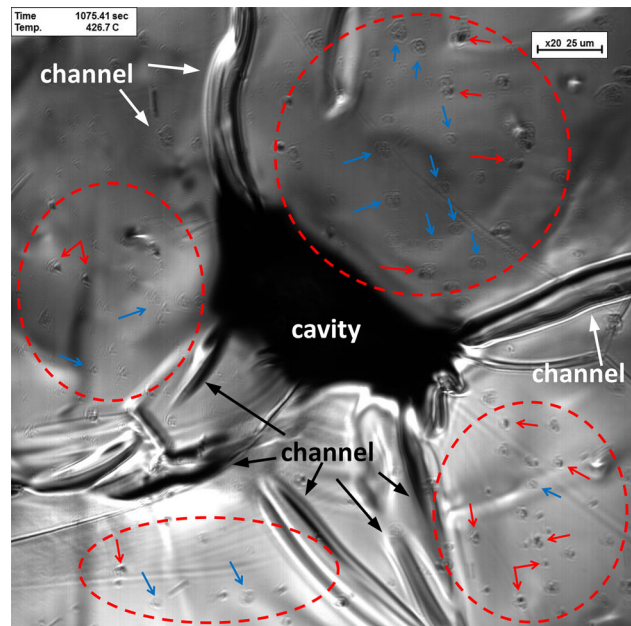

Fig. 11—Reprecipitated fine inclusions in the cooling process (the red arrows refer to the complex inclusions of TiN-MnS, and the blue arrows refer to MnS inclusions) (Color figure online).

inclusion A + C, inclusion B is regarded as a cylinder with a radius of 1 μm, which is grown from 8 to 23 μm in length. Its growth equivalent (calculated in volume) can be regarded as a spherical inclusion grown from 6 to 17 μm in radius. The change of volume is just about half of the amount of volume of inclusion A + C. The reason for this failure to meet the Ostwald ripening reaction is mainly caused by the diffusion of Ti and N which is not completely spread to the inclusion B during the element diffusion process, and half of them diffuse into the molten steel. Therefore, the growth efficiency of inclusion B could not reach the equivalent amount of dissolution of inclusion A + C, and the schematic diagram of element diffusion process is shown in Figure 9. According to the observation of Figures 5(g) through (j), the generation process of long-strip TiN inclusion B was observed in solidification front. Jin et al.[47] have calculated the thermodynamic properties of TiN in medium carbon steel, and they believe that the formation of long-strip TiN is mainly attributed to the high concentration of Ti and N in molten steel. According to the analysis for the Ostwald ripening dissolution of inclusions A + C, the formation of long-strip TiN is caused by the increase of the concentration of Ti and N in a local region due to the dissolution of TiN inclusions in GCr15 bearing steel. The long-strip inclusion B (TiN contained) is generated by the reaction of Ti and N diffusing during the process of Ostwald ripening.

According to the traditional analysis of the TTT curve, it is considered that in the single dissolution process of a inclusion particle, the dissolution of atoms from the particles and the diffusion rate to the surrounding molten steel are uniform, that is, a single TTT dissolution curve for a single dissolution process. To a certain extent, it can reflect the law of material dissolving process. However, in an actual process, with gradually dissolving of the particles, the concentration gradient of Ti and N around the particles has changed. First, the concentration gradient between particles and solvent is large, and the dissolution can be carried out easily. Further, with the increase of the concentration in

matrix and the decrease of the concentration gradient, the dissolution process becomes difficult to be carried out. Therefore, greater superheat is required to maintain the diffusion rate of Ti and N, and the completely dissolving time of the particle is infinite. Hence, the dissolution process of a particle is a non-linear process. Thus, the temperature of the phase transition point increases as the particle size decreases. As mentioned above, employing the multiple TTT curves to characterize a single dissolution process is more consistent with the reality, that is, the multiple TTT dissolution curves for a single dissolution process. Based on the discussion above, the relationship between dissolution of TiN and its size can be formed; the larger the size, the greater the dissolution rate.

In molten steel, a part of Ti and N generated by the dissolution of inclusion A + C will precipitate again as R-I during subsequent solidification, and the precipitation temperature of R-I is approximately 1296 K (1023 °C), as shown in Figure 5(i). As the solidification process continues, the channels around the large inclusion divide the visual field into four areas, as shown in Figure 11. In these areas, the inclusions precipitate in large quantities; the black inclusions precipitate first, and then the gray inclusions precipitate. Some gray inclusions precipitate around the black inclusions wrap them up. According to the previous reports[2,9,48–50] and the thermodynamic calculation of TiN (in this study) and MnS (in previous study)[20] combining the observed experimental phenomena, it can be assumed that the black inclusions are TiN and the gray inclusions are MnS. Around MnS inclusion, manganese-depleted zone (MDZ) will be formed. MDZ has the ability to induce the formation of AF, which can improve the microstructure and properties of steel. Nevertheless, there could be

great differences (components and content, element diffusion, temperature, *etc.*) between high-carbon steel and low-carbon steel at non-equilibrium conditions. The effects of heterogeneous nucleation sites, addition of alloying elements, elements diffusion rate, and nucleation location of inclusions on the microstructure and mechanical properties of the GCr15 bearing steel and other high-carbon steels would be verified by mechanical testing in the further studies.

V. CONCLUSION

In this study, based on the kinetic calculation results, chemical analysis, morphology, and *in situ* observations, the precipitation, aggregation, and dissolution behaviors of the TiN inclusions in GCr15 bearing steel have been studied. The main conclusions are as follows:

1. When [pct Ti] = 0.0078 and [pct N] = 0.0049, the precipitation temperature is between 1640 K and 1680 K and the local cooling rate is between 0.5 K/s and 10 K/s. The single-particle TiN inclusion can precipitate only after the solid fraction is higher than 0.847, and its precipitation radius is between 1 and 6 μm, which can be reduced by decreasing the N content in steel and increasing the cooling strength.
2. The aggregation and densification mechanisms of the multi-particle aggregated TiN inclusions are verified by CLSM observation and theoretical analysis. The aggregation and densification mechanisms described as TiN inclusions are adsorbed and aggregated to each other by CBF. After collision, the inclusions and new precipitates are sintered in solid-phase state. The results of the stress analysis show that the CBF plays a dominant role in the aggregation process of inclusions.
3. It is observed by FE-SEM with EDS and CLSM that TiN has a small amount of solid-solution element, V, and their atomic ratio is approximately 18:1, which may lead to the melting of inclusion and forming the liquid (Ti,V)N inclusion at an approximate temperature of 1688 K (1415 °C).
4. The dissolution of TiN inclusions is positively related to the size of the inclusions: the larger the size, the greater the dissolution rate. The long-strip TiN inclusion may be formed by the Ostwald ripening of two TiN inclusions. The TiN inclusions smaller than 3 μm in the GCr15 bearing steel may be formed by the T̲i̲ and N̲ dissolved by TiN.

REFERENCES

1. W. Ma, Y. Bao, L. Zhao, and M. Wang: *Int. J. Mine. Metall. Mater.*, 2014, vol. 21, pp. 234–39.
2. Y. Liu, L. Zhang, H. Duan, Y. Zhang, Y. Luo, and A.N. Conejo: *Metall. Mater. Trans. A*, 2016, vol. 47A, pp. 3015–25.
3. H.Y. Liu, H.L. Wang, L. Li, J.Q. Zheng, Y.H. Li, and X.Y. Zeng: *Ironmak. Steelmak.*, 2013, vol. 38, pp. 53–58.
4. J. I. Takamura, and S. Mizoguchi: *Proc. Int. Iron and Steel Congr., 6th*, 1990, pp. 591–97.
5. H. Ohta, R. Inoue, and H. Suito: *ISIJ Int.*, 2008, vol. 48, pp. 294–300.
6. X. Yin, Y. Sun, Y. Yang, X. Bai, M. Barati, and A. Mclean: *Metall. Mater. Trans. B*, 2016, vol. 47B, pp. 3274–84.
7. W. Yan, Y. Shan, and K. Yang: *Metall. Mater. Trans. A*, 2006, vol. 37A, pp. 2147–58.
8. S. Kanazawa, A. Nakashima, K. Okamoto, and K. Kanaya: *Armaghan Danesh*, 1975, vol. 61, pp. 130–40.
9. Y. Tomita, N. Saito, T. Tsuzuk, Y. Tokunaga, and K. Okamo: *ISIJ Int.*, 1994, vol. 34, pp. 829–35.
10. M.A. Linaza, J.L. Romero, J.M. Rodriguez-Ibabe, and J.J. Urcola: *Scripta Metall. Mater.*, 1993, vol. 29, pp. 451–56.
11. H. Todoroki, and N. Shiga: *Proceedings of the International Congress on Science and Technology of Steelmaking*, ISIJ, Tokyo, Japan, 2008, pp. 121–24.
12. K. Oikawa, H. Ohtani, K. Ishida, and T. Nishizawa: *ISIJ Int.*, 1995, vol. 35, pp. 402–08.
13. S. Mukae, K. Nishio, M. Katoh, and T. Isayama: *J. Jpn. Weld Soc.*, 1985, vol. 3, pp. 567–74.
14. H. Mabuchi, R. Uemori, and M. Fujioka: *ISIJ Int.*, 1996, vol. 39, pp. 1406–12.
15. M. Fattahi, N. Nabhani, M. Hosseini, N. Arabian, and E. Rahimi: *Micron*, 2013, vol. 45, pp. 107–14.
16. P. Misra, S. Sridhar, and A.W. Cramb: *Metall. Mater. Trans. B*, 2001, vol. 32B, pp. 963–67.
17. Y. Zhang, X. Li, and H. Ma: *Metall. Mater. Trans. B*, 2016, vol. 47B, pp. 2148–56.
18. X. Wan, B. Zhou, K.C. Nune, Y. Li, K. Wu, and G. Li: *Sci. Technol. Weld. Join.*, 2016, vol. 22, pp. 343–52.
19. L. Yang, G. Cheng, S. Li, M. Zhao, and G. Feng: *ISIJ Int.*, 2015, vol. 55, pp. 1901–05.
20. Q. Tian, G. Wang, Y. Zhao, J. Li, and Q. Wang: *Metall. Mater. Trans. B*, 2018, vol. 49B, pp. 1149–64.
21. H. Suito and H. Ohta: *ISIJ Int.*, 2006, vol. 46, pp. 33–41.
22. G.M. Gulliver: *Metallic Alloys*, Griffen, London, 1922.
23. E. Scheil: *Zeitschrift Metallkunde*, 1942, vol. 34, pp. 70–72.
24. E. Gao, G. Zou, W. Wang, F. Ma, and X. Luo: *Metall. Mater. Trans. B*, 2017, vol. 48B, pp. 1014–23.
25. Y. Won and B.G. Thomas: *Metall. Mater. Trans. A*, 2001, vol. 32A, pp. 1755–67.
26. F. Huang, J. Zhang, X. Wang, S. Wang, Y. Fang, and Y. Yu: *J. Iron Steel Res.*, 2008, vol. 20, pp. 14–19 (in Chinese).
27. K. Sasai: *ISIJ Int.*, 2016, vol. 56, pp. 1013–22.
28. K. Sasai: *ISIJ Int.*, 2014, vol. 54, pp. 2780–89.
29. M. Nakamoto, T. Tanaka, M. Suzuki, K. Taguchi, Y. Tsukaguchi, and T. Yamamoto: *ISIJ Int.*, 2014, vol. 54, pp. 1195–203.
30. R.N. Lumley, T.B. Sercombe, and G.M. Schaffer: *Metall. Mater. Trans. A*, 1999, vol. 30A, pp. 457–63.
31. C. Xuan, A.V. Karasev, P.G. Jönsson, and K. Nakajima: *Steel Res. Int.*, 2016, vol. 87, pp. 1–9.
32. K. Wu: *Principles of Metallurgical Transport*, 1st ed., Metallurgical Industry Press, Beijing, 2011, p. 7.
33. Y. Sui, G. Sun, Y. Zhao, C. Wang, M. Guo, and M. Zhang: *J. Univ. Sci. Technol. Beijing*, 2014, vol. 36, pp. 1174–82.
34. L. Zhang, C. Guo, W. Yang, Y. Ren, and H. Ling: *Metall. Mater. Trans. B*, 2018, vol. 49B, pp. 803–11.
35. W. Ostwald: *Lehrbuch der Allgemeinen Chemie*, 1896, Vol. 2.

36. W. Ostwald: *Zeitschrift Für Physikalische Chemie*, 1897, vol. 22, pp. 289–330.
37. R. Tadmor: *J. Phys. Cond. Matter*, 2001, vol. 13, pp. 195–202.
38. I.M. Lifshitz and V.V. Slyozov: *J. Phys. Chem. Solids*, 1961, vol. 19, pp. 35–50.
39. C. Wagner: *Zeitschrift für Elektrochemie*, 1961, vol. 65, pp. 581–91.
40. H.B. Aaron: *Metal Sci.*, 1968, vol. 2, pp. 192–93.
41. L. Cheng, E. Hawbolt, and T. Meadowcroft: *Metall. Mater. Trans. A*, 2000, vol. 31A, pp. 1907–16.
42. J. Moon, C. Lee, S. Uhm, and J. Lee: *Acta Mater.*, 2006, vol. 54, pp. 1053–61.
43. T. Hong and T. Debroy: *Metall. Mater. Trans. B*, 2003, vol. 34B, pp. 267–69.
44. T. Hong and T. Debroy: *Ironmak. Steelmak.*, 2001, vol. 28, pp. 450–54.
45. T. Hong and T. Debroy: *Scripta Mater.*, 2001, vol. 44, pp. 847–52.
46. M.J. Whelan: *Met. Sci. J.*, 1969, vol. 3, pp. 95–97.
47. Y. Jin, and S. Du: *Ironmak. Steelmak.*, 2016, published online, pp. 1–6.
48. S. Lee, Y. Oh, and K. Yi: *Mater. Trans.*, 2002, vol. 43, pp. 518–22.
49. Y. Chen, Y. Bao, M. Wang, X. Cai, L. Wang, and L. Zhao: *ISIJ Int.*, 2014, vol. 54, pp. 2215–20.
50. P. Chen, C. Zhu, G. Li, Y. Dong, and Z. Zhang: *ISIJ Int.*, 2017, vol. 57, pp. 1019–28.